

# **Analysis of the microstructure of injection moulded polymeric heart valve leaflets**

Name: Spyros Ploussiou

University: University of Cambridge

College: Wolfson College

Project colleague: Achilleas Papadimitriou

Project supervisors:

Dr. Joanna Stasiak & Prof. Geoff Moggridge

Date: 14/05/2021

# Impact of Covid-19

In addition to analysis of X-ray data, between October and November 2020, significant efforts were made to experimentally investigate the bio-stability and mechanical properties of various polymers. These experiments were initiated but not completed due to lab closures. The experimental procedure is outlined below:

- Thin discs of specific polymers that are candidates for use in polymeric heart valve leaflets, were prepared by compression moulding and solvent casting.
- To test the bio-stability of these samples, aqueous solutions of 20 wt. %  $\text{H}_2\text{O}_2$  and 0.1 mol  $\text{dm}^{-3}$  of solid  $\text{CoCl}_2$  were prepared. These solutions represent the oxidative environment in the native aorta.
- In order to make the aforementioned solutions, 10.99 g of  $\text{CoCl}_2$  were initially added to 400 ml of de-ionised water, in a glass water bottle. Then, 600 ml of  $\text{H}_2\text{O}_2$  were slowly added. The slow addition was performed due to, the rigorous and exothermic nature of the reaction between aqueous  $\text{H}_2\text{O}_2$  and solid  $\text{CoCl}_2$ .
- The solvent cast polymer discs were placed in tightly sealed glass bottles, each containing 100 ml of the prepared solutions. The glass bottles were then placed in a water bath and maintained at 37 °C, for 4 weeks. The methodology is suitable for accelerated oxidation testing and follows the study reported by Christenson et al., 2004.

The polymers employed in the oxidative degradation tests are listed in Table 1.

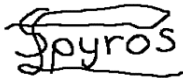
Table 1: List of polymers that were solvent cast for oxidative degradation experiments.

Polymer	Name of supplier	Styrene wt. %
Polyurethane	Kaneka	-
SIBSTAR	Kaneka	15
SIBSTAR	Kaneka	22.5
SIBSTAR	Kaneka	30
SEBS	Kraton	22
SEBS	Kraton	29
SEBS	Septon	30
SEBS	Septon	18

The Structured Materials group at the Department of Chemical Engineering and Biotechnology of the University of Cambridge, is continuing this experimental work. The aim is to carry out gel permeation chromatography (GPC) and fourier-transform infrared spectroscopy (FTIR) on the samples, following the process of oxidative degradation. This will yield data pertaining to any physical changes the samples may have undergone during the process of oxidative degradation. Due to lab closures, our IIB project focused entirely on analysis of synchrotron data.

# Preface

The work described in this report is the result of my own research, unaided except as specifically acknowledged in the text, and it does not contain material that has already been used to any substantial extent for a comparable purpose. This report contains 38 pages and 10 000 words (excluding this page).

Signature:   
Spyros

Date: 14/05/2021

# Summary

Heart valve replacement by means of surgery, remains the most effective treatment of aortic heart valve disease. Polymeric heart valve prostheses comprising of styrene-based thermoplastic block copolymers show great promise for use in cardiovascular applications. The process of injection moulding can lead to anisotropy in the microstructure of such polymers. This anisotropy can mimic that found in the native aortic heart valve.

The microstructure of a specific thermoplastic block copolymer referred to as SEPS, with a styrene weight fraction of 0.22, was analysed during the process of injection moulding and post-injection moulding by means of synchrotron Small Angle X-ray Scattering. Regardless of the annealing conditions employed during the injection moulding process, the microstructure displayed extremely good orientation and negligible residual stresses. These characteristics are paramount in ensuring that, the heart valve replacements exhibit extremely good and anisotropic mechanical properties. Such characteristics also influence the hydrodynamic properties of the heart valve prostheses.

Furthermore, the anisotropy in microstructure of SEPS attained, post-injection moulding, was found to be adequately predicted by a polymer chain orientation model and a simple generalised Newtonian, power law constitutive relation with a power law exponent of 0.53.

# Contents

<b>1</b>	<b>Introduction</b>	<b>6</b>
1.1	Background on heart valve replacements . . . . .	6
1.2	Motivation for development of PHVs . . . . .	6
1.3	Challenges in developing PHVs . . . . .	7
1.4	Thesis outline . . . . .	8
<b>2</b>	<b>Literature review</b>	<b>9</b>
2.1	Polymers in heart valve replacements . . . . .	9
2.1.1	Types of polymers . . . . .	9
2.1.2	Styrene-based TBCP microstructure and self assembly . . . . .	9
2.1.3	Polymer characterisation techniques . . . . .	10
2.2	Injection moulding manufacturing process . . . . .	10
2.2.1	Process parameters and process modelling . . . . .	10
2.2.2	Flow dynamics during injection moulding . . . . .	11
2.2.3	Annealing during injection moulding . . . . .	11
<b>3</b>	<b>Methods</b>	<b>12</b>
3.1	Experimental . . . . .	12
3.1.1	Data acquisition . . . . .	12
3.1.2	Data processing . . . . .	13
3.1.3	Sources of error . . . . .	14
3.2	Theoretical . . . . .	15
3.2.1	Skin and core oriented cylindrical domains . . . . .	15
3.2.2	Degree of orientation of cylindrical domains . . . . .	17
3.2.3	$d$ -spacing of cylindrical domains . . . . .	18
<b>4</b>	<b>Results and discussion</b>	<b>20</b>
4.1	Skin and core oriented cylindrical domains . . . . .	20
4.1.1	Experimentally determined and predicted volume fractions . . . . .	20

4.1.2	Influence of processing parameters on skin layer volume fraction . . . . .	21
4.2	Degree of orientation of cylindrical domains . . . . .	25
4.2.1	Influence of processing parameters on degree of orientation . . . . .	25
4.3	<i>d</i> -spacing of cylindrical domains . . . . .	27
4.3.1	Influence of processing parameters on <i>d</i> -spacing . . . . .	27
<b>5</b>	<b>Conclusions and recommendations</b>	<b>29</b>
5.1	Conclusions . . . . .	29
5.2	Recommendations . . . . .	29
<b>References</b>		<b>29</b>
<b>Appendix A</b>		<b>32</b>
<b>Appendix B</b>		<b>33</b>
<b>Nomenclature</b>		<b>36</b>

# Chapter 1

## Introduction

### 1.1 Background on heart valve replacements

Heart valve disease is a combination of factors that compromise the cardiovascular system. These include heart valve stenosis and regurgitation. Stenosis occurs when the area available for physiological blood flow by the opening valve is reduced whereas, regurgitation is when the heart valve fails to restrict blood flow reversal [1].

Heart valve disease can lead to heart failure, in which case, death is typically a result of cardiac arrest and stroke. The Euro Heart Survey reports that the majority of valvular disease is aortic, with a disease incidence of 44.3 %. Heart valve replacement by surgical means remains the most effective treatment of valvular disease, especially aortic. On a global scale, between 270 000 and 370 000 heart valve replacements occur annually [2], and these are predicted to reach 890 000 by 2050 [3]. The most common types of heart valve replacements are bio-prosthetic and mechanical.

Bio-prosthetic valves have limited durability and a usual lifespan of 10 - 15 years, in a host. Mechanical valves are more durable but, require anticoagulation therapy [4].

Polymeric heart valve (PHV) prostheses are being extensively tested in pre-clinical trials, and offer the possibility of combining the good durability of mechanical valves and exceptional bio-compatibility of bio-prosthetic valves.

### 1.2 Motivation for development of PHVs

Nowadays, a lot of efforts are underway to develop a viable PHV for cardiovascular applications. They have the potential of being cheaper and faster to manufacture than bio-prosthetic and mechanical valves [5].

Figure 1.1 depicts the microstructural components of the native aortic heart valve and the configuration they attain during cardiac systole and diastole, respectively.

The unique microstructure of the native aortic heart valve grants its strength and flexibility. The ability to mimic this behaviour lies at the forefront of current efforts in the development of PHVs. Certain polymers have been demonstrated to closely mimic this behaviour [6].

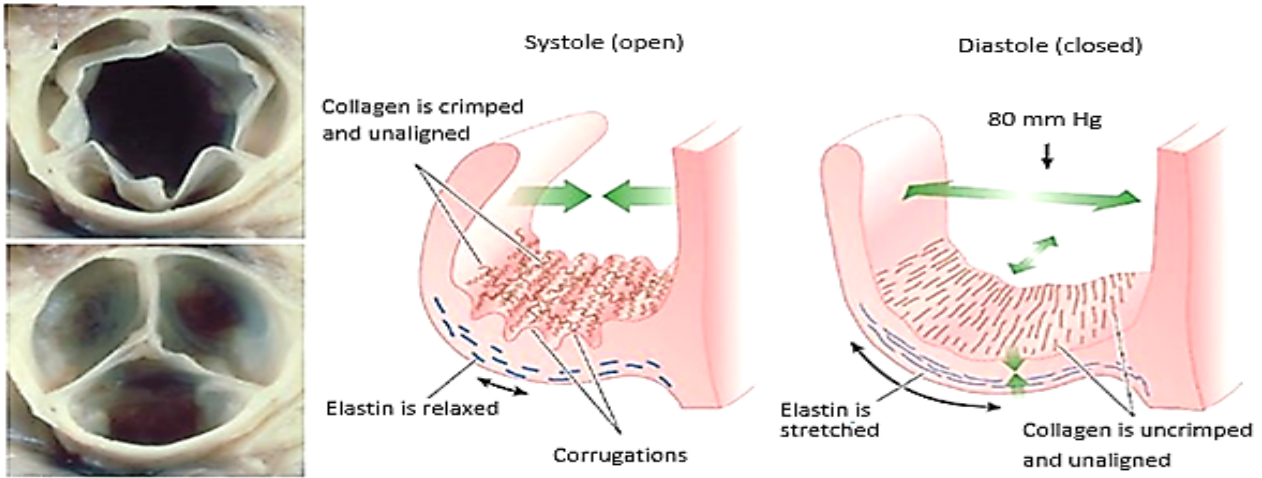


Figure 1.1: Schematic of aortic heart valve during systole and diastole [7].

### 1.3 Challenges in developing PHVs

There is a plethora of parameters that must meet certain criteria, if a device intended for use as a heart valve prosthetic is to reach clinical trials. The parameters can be bundled in terms of their influence on the bio-stability, bio-compatibility, haemocompatibility, hydrodynamic and mechanical behaviour of the heart valve prosthesis. These aspects are coupled, and optimisation of the performance of the heart valve involves finding a balance between their respective performances.

In addition, achieving the optimal heart valve geometry is also critical towards the design of a viable heart valve prosthesis. Many studies show that, the tri-leaflet aortic valve prosthetic with a central orifice bears the most similar flow dynamics to the native aortic heart valve. As a matter of fact, the latest PHV manufactured by the Structured Materials group at the Department of Chemical Engineering and Biotechnology in Cambridge, embodies the aforementioned design. Figure 1.2 depicts the features of this PHV.

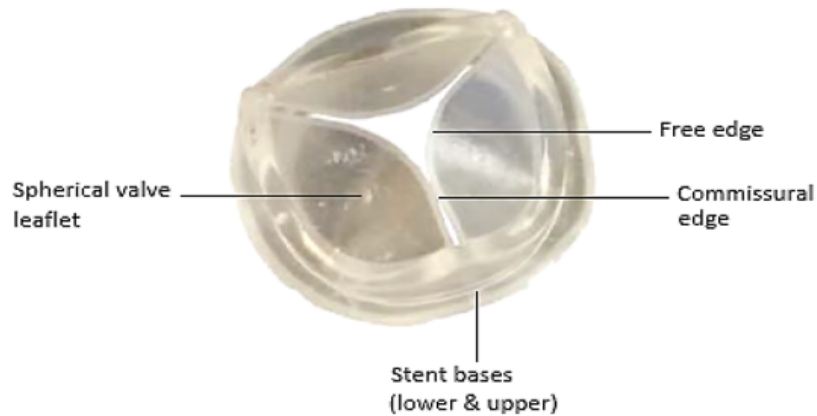


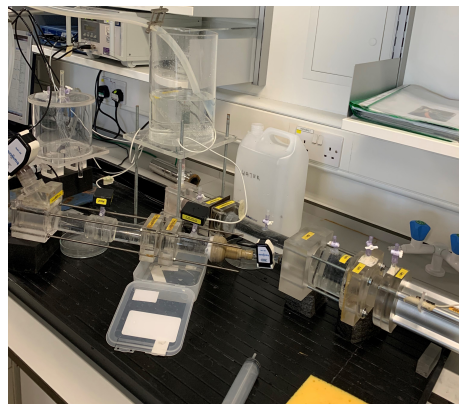
Figure 1.2: Schematic of characteristics of PHV.

The spherical leaflet geometry of the valve was determined by optimising the stresses it endures, during opening and closure [8].

The hydrodynamic and mechanical behaviour of the valves manufactured by the Structured Materials group are tested in vitro using bench-scale equipment. Hydrodynamic testing is essential for quantifying critical parameters of valve performance such as, the percentage of back flow experienced by the valve. Accelerated fatigue testing is conducted as well, to quantify the number of cycles, analogous to systole and diastole, sustained by the heart valves prior to failure. Figure 1.3 depicts the equipment used for these purposes [9].



(a) Fatigue testing.



(b) Hydrodynamic testing.

Figure 1.3: Equipment used to test the mechanical (1.3a) and hydrodynamic (1.3b) behaviour of the PHVs.

The microstructural characteristics of the components of the PHVs, play a critical role in determining their mechanical and hydrodynamic properties mainly. The process of injection moulding and use of thermoplastic block copolymers (TBCPs) with polystyrene glassy domains, lead to the manufacture of products with distinctive anisotropy, which can be exploited to optimise the overall performance of PHVs [10].

## 1.4 Thesis outline

The main objective of this thesis is to analyse the microstructural characteristics attained by a specific TBCP, during the process of injection moulding and post-injection moulding. The TBCP is intended for use in polymeric heart valve leaflets by the Structured Materials group at the Department of Chemical Engineering and Biotechnology in Cambridge. Aspects such as residual stresses and degree of orientation, resulting from processing of the material, are explored.

In the remainder of this thesis, the information gathered from the literature regarding the microstructure of TBCPs and its characterisation is critically reviewed. The information gathered with reference to the process of injection moulding is also reviewed. Furthermore, the methods employed to analyse the microstructural evolution of different samples of the TBCP during and following injection moulding are mentioned. Finally, the results of the analyses are presented and discussed, and where possible, conclusions are drawn.

# Chapter 2

## Literature review

### 2.1 Polymers in heart valve replacements

#### 2.1.1 Types of polymers

Polyurethanes have been the most commonly used type of polymer for cardiovascular applications, owing mainly to their good haemocompatibility and durability. However, studies show that they tend to fail due to bad calcification which leads to unacceptable degrees of regurgitation [11]. Regurgitation is usually associated with valve design.

Thermoplastic block copolymers (TBCPs) and particularly, styrene based TBCPs, show great promise for use in heart valve replacements. They can attain various microstructural morphologies under different conditions. Physical properties such as, their polydispersity index and average molecular weight, can be tailored to more closely mimic properties of collagen and elastin in the native aortic heart valve. In addition, the processing conditions imposed during their manufacturing can be tuned to achieve distinct anisotropy.

Typical styrene-based TBCPs include [12]:

- poly(styrene-*block*-ethylene/propylene-*block*-styrene) referred to as SEPS.
- poly(styrene-*block*-ethylene/butylene-*block*-styrene) referred to as SEBS.

SEPS is the TBCP, for which the microstructure and its evolution during and following injection moulding, are analysed in this thesis.

#### 2.1.2 Styrene-based TBCP microstructure and self assembly

Styrene-triblock-copolymers consist of polystyrene glassy domains surrounded by an elastomeric phase. This type of microseparation is governed by thermodynamics, in the absence of kinetic limitations. The Flory Huggins thermodynamic model is extensively used to describe the microseparation process. Key parameters involved in this microstructural phenomenon include, the average molecular weight and weight fraction of the styrene fraction in the polymer blend [13].

As far as glassy and rubbery domains in microseparated styrene-triblock-copolymers are concerned, in the scenario that the 2 polymers are present in equal volume fractions, the interface

between them is flat, and the larger the difference in their volume fractions, the more asymmetric and curved the interface becomes. These interfacial phenomena and the ways in which they are affected by the physical properties of the polymer constituents, give rise to a variety of microstructural arrangements.

Styrene-based TBCPs form cylindrical hard domains, when the styrene weight fraction in the copolymer blend is in the range 20 - 30 %. Below 20 and above 30 %, they tend to form spherical and lamellar glassy domains, respectively. This in effect signals that, the weight fraction of this type of TBCPs can be adjusted to tune the flexibility of manufactured components [14].

The self assembly of styrene based TBCPs into cylindrical hard domains with styrene weight fraction in the range 20 - 30 %, can be exploited for the purposes of producing polymeric components with distinct anisotropy in the orientation of the cylinders, which can mimic collagen and elastin in the native heart valve tissue.

### 2.1.3 Polymer characterisation techniques

Common analytical techniques employed to characterise the microstructure of styrenic TBCPs include Transmission Electron Microscopy (TEM), synchrotron Small Angle X-ray Scattering (SAXS), Fourier-Transform Infrared Spectroscopy (FTIR) and Gel Permeation Chromatography (GPC).

As far as this thesis is concerned, the technique employed to monitor the evolution in microstructure of SEPS, during and following injection moulding was SAXS.

SAXS is a powerful tool for monitoring microstructural changes in polymers, because the wavelength  $\lambda$  of X-rays is comparable to the atomic-spacing in the polymeric structures. In SAXS analysis, a lot of assumptions such as that of the volume of material being irradiated remaining constant, are made. This may be invalid, particularly when an irradiated sample is subject to stresses causing shrinkage or expansion [15].

SAXS involves synchrotron equipment where, subatomic particles are accelerated to high speeds. They emit high energy X-rays, which are collimated and focused towards a target sample. The X-rays striking the target sample, are scattered by parallel atomic, close packed planes, defined by the miller indices  $h$ ,  $k$  and  $l$ . These form the basis of bravais lattice types, and SAXS data can yield information on the interplanar spacing ( $d$ -spacing) between pairs of parallel ( $hkl$ ) planes [15].

## 2.2 Injection moulding manufacturing process

### 2.2.1 Process parameters and process modelling

Injection moulding is a process whereby, rapid manufacturing of material components can be achieved. A simple injection moulding machine consists of a chamber in which an extruder is positioned, where the material of interest is inserted in granular or powder form. The material is then melted and attains its melt temperature  $T_m$ . It is then injected into the mould chamber where it attains its mould temperature  $T_{mould}$ . The process itself is complex and involves coupling of partial differential equations which encompass the equation of state of the material

being processed, its constitutive rheological relationship, conservation equations and equations describing the orientation in the microstructure of the material being processed. Many studies have been conducted to, accurately model this process and prevent any anisotropy in resultant material microstructure it may lead to. This is the opposite of what is desired for use in PHVs. Moreover, numerous studies are being performed using Artificial Neural Networks and statistical methods such as the Taguchi method to optimise and isolate the most important process parameters in injection moulding. These parameters obviously vary depending on the desired outcome of the process. Yet, these methods have proven to be useful in minimising trial and error experiments and predicting optimal parameter ranges for future experiments [16, 17].

### 2.2.2 Flow dynamics during injection moulding

With reference to the TBCP SEPS analysed in this thesis, different conditions were examined during injection moulding. These include the stages of annealing and cooling. It must also be noted that, some samples of SEPS were subjected to cooling, but not annealing.

The packing stage, which is common in injection moulding and involves uniform packing pressure across the mould, post-filling, was not performed on the SEPS samples analysed. Only the filling stage of injection moulding is relevant to the analysis conducted in this thesis. During the filling stage, complex flow dynamics lead to a region in which fountain flow occurs. This region is associated with the melt front in the mould, and numerous studies to model its shape and size using computational fluid dynamics (CFD) and polar-gridline transformations were conducted in the past. The melt front involves extensional flow fields ahead of shear flow fields [18, 19].

The complex phenomenon of fountain flow, plays an important role in influencing the flow induced and thermal stresses in injection moulded styrenic TBCPs. They may act as residual stresses, influencing the anisotropy in mechanical properties of the injection moulded product. In addition, cooling rate plays a very important role at the flow front region and the temperature distribution associated with it.

### 2.2.3 Annealing during injection moulding

No records were found in the literature regarding the effects of annealing on injection moulded styrenic-triblock TBCPs. Annealing is usually associated with the removal of microstructural defects. In addition, this process tends to remove any residual stresses in the processed polymer. The important parameters in annealing are, annealing temperature and annealing time. These influence defect density, grain size and  $d$ -spacing [20].

Regarding styrenic-diblock TBCPs with cylindrical microstructure, studies show that grain size tends to increase with both annealing temperature and annealing time. On the contrary,  $d$ -spacing is only significantly affected by annealing temperature.  $d$ -spacing tends to decrease with increasing annealing temperature but, remains relatively unaffected with changes in annealing time [20, 21, 22]. However, it must be noted that the aforementioned studies were performed on either solvent cast or extruded styrenic-diblock TBCPs, as opposed to injection moulded ones.

# Chapter 3

## Methods

### 3.1 Experimental

#### 3.1.1 Data acquisition

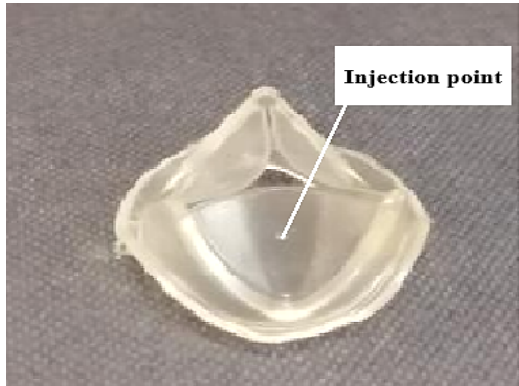
The SAXS data relevant to the analysis of the microstructure of SEPS with a styrene weight fraction of 0.22, was collected by the Structured Materials group, using the synchrotron beam line I22 [23]. The first experiment was a series of in-situ SAXS measurements during injection moulding of SEPS. The energy of the X-ray beam was 17 keV, and the beam covered an area equivalent to  $22\,500\,\mu\text{m}^2$ . The sample-detector distance was 3.4 m. A bench-scale mini-extruder adapted to fit the synchrotron beam line was used for the in-situ experiment.

Molten samples of SEPS were injected at a speed of  $2\,\text{mm s}^{-1}$  by a piston of diameter 0.015 m, between 2 parallel aluminium plates. The volumetric flowrate  $Q$  of the molten SEPS was  $0.35\,\text{cm}^3\,\text{s}^{-1}$ . The mini-extruder was mounted on a moving stage, allowing the X-ray beam to map the sample from the injection point to its edge. The temporal resolution of the X-ray scans was 5 s. In another set of measurements, the extruder was kept at a fixed position, closest to the injection point, which allowed for observation of the microstructure evolution during flow, at a single point in the sample.

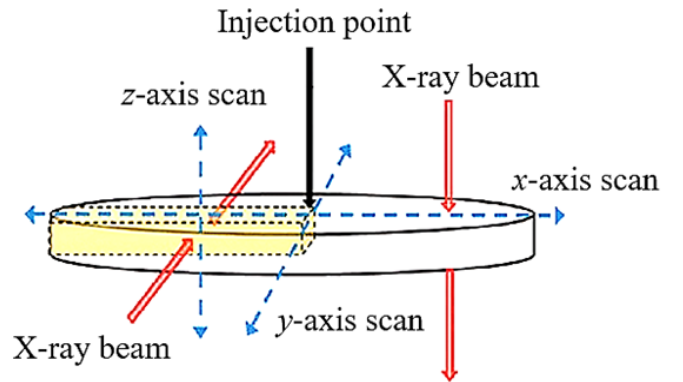
The main objective of this experiment, referred to as the  $z$ -axis scan, was to study the effects of annealing, cooling rate and flowrate on the microstructure generated within the sample. The injection temperature was kept constant at 453 K, by heating the aluminium mould plates. The cooling time for all samples, at the end of the injection moulding process, was 20 minutes, on average.

The second experiment was conducted post-injection moulding. In this case,  $x$  and  $y$  direction X-ray scans were performed. These are termed the microfocus data. The energy and radius of the beam were 14 keV and  $13\,\mu\text{m}$ , respectively. The sample-detector distance was 1.0 m. The  $x$ -axis scans were performed across the thickness of the samples at 12, 27 and 42 mm from the injection point. The  $y$ -axis scans were performed at a distance of 42 mm from the injection point only. Tables 5.1 and 5.2 in Appendix A, list the thicknesses and annealing conditions for the  $x$ -axis and  $y$ -axis scanned samples, respectively.

In addition, Figure 3.1 depicts both the position of the injection point with respect to the tri-leaflet PHV, and a schematic of the injection moulded disc samples and X-ray scans performed on them.



(a) PHV manufactured.



(b) Sample discs prepared.

Figure 3.1: (3.1a) depicts the position of the injection point relative to the PHV leaflets. (3.1b) depicts a schematic of the disc geometry of the SEPS samples, and the X-ray scans performed on them.

### 3.1.2 Data processing

The SAXS data for  $x$ ,  $y$  and  $z$  axis scans were converted to red-green-blue (RGB) images via the DawnDiamond version 2.21 software package. Figure 3.2 depicts typical SAXS images observed during the analysis.

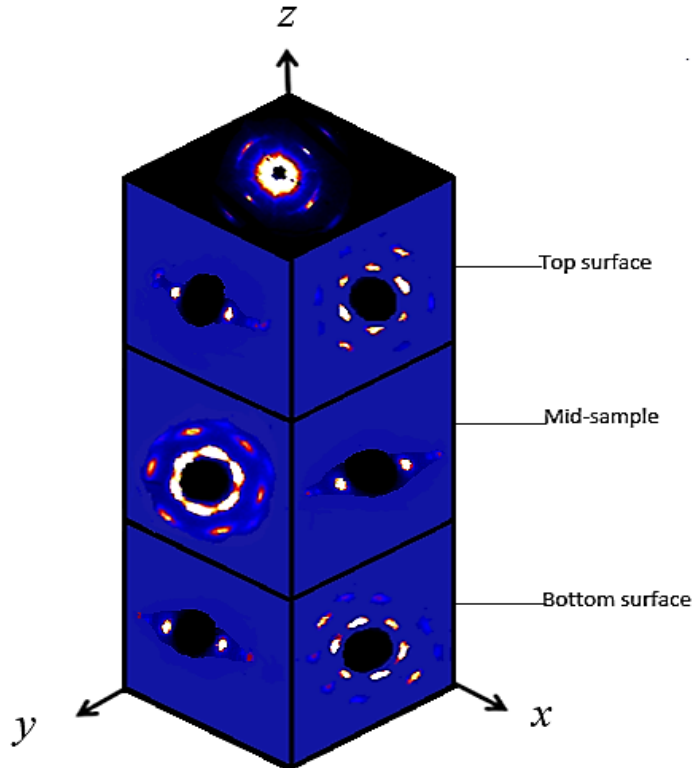


Figure 3.2: Schematic of SAXS images analysed for each of  $x$ ,  $y$  and  $z$  axis scans.

DawnDiamond version 2.21 has pre-set processing commands as well as, basic Python and Java interfaces. Azimuthal,  $\phi$ , and polar,  $\theta$ , angle intensity as well as  $d$ -spacing calculations were performed using this software. Calibration with a standard reference material, was necessary. However, the latest version of DawnDiamond lacks some of the processing capabilities necessary to fully analyse the data and automate the process. As a result, the data were systematised in Excel files and exported to Python for further analysis. The majority of the time was spent developing algorithms in Python to analyse approximately 20 000 SAXS images for  $x$  and  $y$  axis scans and 10 000 SAXS images for  $z$ -axis scans. The spatial resolution between  $x$  and  $y$  axis scan images was 10  $\mu\text{m}$ . The temporal resolution between  $z$ -axis scan images was 5 s.

The SAXS images required pre-processing prior to analysis. There was a lot of noise in the data due to background intensity and intensity flashes arising from X-rays striking the aluminium mould plates, in the case of the  $z$ -axis scan data. These flashes obscured some of the diffraction patterns. A data cleaning procedure was implemented, as also detailed below:

- Data pertaining to the  $2\theta$ ,  $\phi$  intensity and  $d$ -spacing profiles of the SAXS images were arranged in dataframes in Python. This was performed to allow manual data cleaning, where deemed necessary.
- The background noise in the data was removed automatically by identifying and subtracting the minimum most possible intensity value, in each data-set.
- A set of conditional statements was devised in Python for each set of SAXS images, to remove the majority of the noise arising from the intensity flashes. A peak finding algorithm was also implemented for the purposes of automating this process.
- The resultant data from the pre-processing steps were fitted against polynomial curves using the maximum capacity of the Singular Value Decomposition implementation of the Python SciPy library. This was preferred against Gaussian curve fitting algorithms. Polynomial regression was more sensitive in picking up any remaining intensity noise in the data.
- In spite of these efforts, some of the data were obscured to such great extent that their recovery was not possible.

### 3.1.3 Sources of error

As far as the microfocus data are concerned, a main source of error was that of the X-ray beam size of 13  $\mu\text{m}$ . This was similar to the spatial resolution of the X-ray scans of 10  $\mu\text{m}$ . This led to overlap in the area being irradiated, between consecutive SAXS image frames, and introduced uncertainty in any measurements conducted.

Another major source of error was that due to, the noise arising from the background intensity in the SAXS measurements and intensity flashes from X-rays striking the aluminium mould plates, especially for the  $z$ -axis scan data. In spite of the fact that, a data cleaning procedure was implemented, these still contributed, in part, to the uncertainties associated with any measurements performed.

## 3.2 Theoretical

### 3.2.1 Skin and core oriented cylindrical domains

Anisotropy in injection moulded TBCPs was previously demonstrated by the Structured Materials group. Two different layers across the thickness of the samples are formed, of radially and circumferentially oriented cylindrical domains, as also shown in Figure 3.3. These mainly arise due to, the dominance of extensional flow fields and shear flow fields in the core and surface layers of the cylindrical disc samples, respectively.

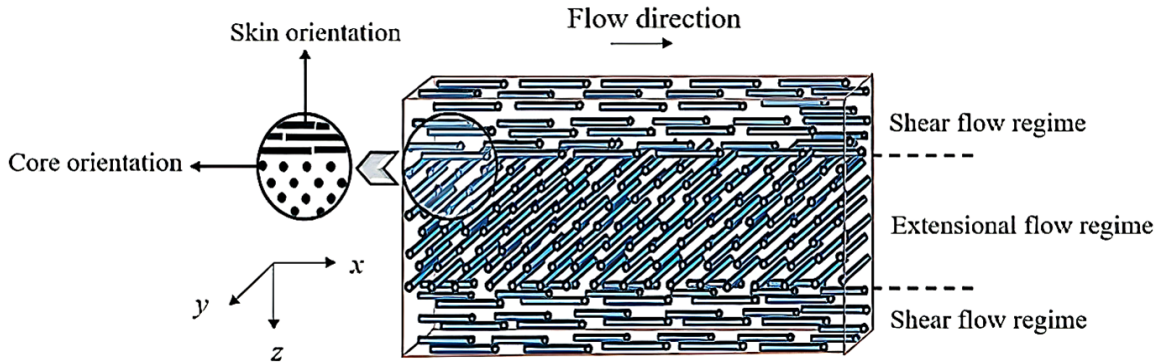


Figure 3.3: Schematic of alignment of cylindrical microstructure across disc sample thickness [6].

The cylindrical domain, when viewed parallel to the axis of symmetry of the cylinders, displays a hexagonal diffraction pattern in SAXS images. The hexagonal packing of the cylinders gives rise to the possibility of 1<sup>st</sup> order,  $\sqrt{3}$ , 2<sup>nd</sup> order,  $\sqrt{7}$ , 3<sup>rd</sup> order,  $\sqrt{12}$  and 4<sup>th</sup> order,  $m$ , diffraction patterns [24]. With reference to the SAXS images analysed in this thesis, the skin and core oriented cylindrical domains, displayed a hexagonal diffraction pattern in the  $x$ -axis and  $y$ -axis scans of the microfocus data, respectively.

As far as the  $z$ -axis scans are concerned, the skin and core oriented domains were identified as diffraction patterns, as depicted in Figure 3.4. The skin oriented domains correspond to the diffraction spots at  $\phi$  of 0° and 180° whereas, the core oriented domains correspond to the diffraction spots at  $\phi$  of 90° and 270°.

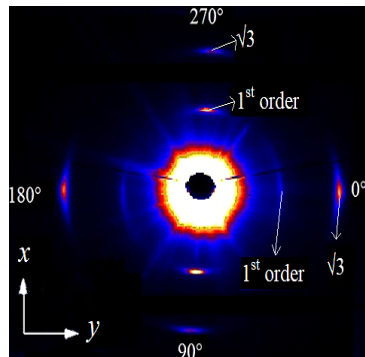


Figure 3.4: Example  $z$ -axis scan SAXS image and position of  $\sqrt{3}$  and 1<sup>st</sup> order diffraction spots.

The thickness of the skin and core layers was estimated by use of 3 methods. In the first method, the microfocus data were employed. Total azimuthal integrated intensities of the overall intensity and that of the 1<sup>st</sup> order and  $\sqrt{3}$  diffraction spots, were performed in Python. It was observed that, as far as the  $\sqrt{3}$  diffraction spots are concerned, these only appeared for the hexagonal diffraction patterns, namely for skin orientation in the *x*-axis scans and core orientation in *y*-axis scans.

In the second method, the number of SAXS image frames corresponding to hexagonal as opposed to 2 - spot diffraction patterns, was measured against the number of all frames in each of the *x*-axis and *y*-axis scans. As a result, estimates of the skin volume fractions at each position from the injection point were made by, dividing the number of frames analogous to the hexagonal diffraction pattern by, the total number of frames in each *x*-axis scan.

In essence, both methods employed a frame count strategy. It is well understood that this is only an approximation of the fraction of the thickness of each layer, and in one dimension. As a result, to confirm that these estimates were reasonable, a 3<sup>rd</sup> methodology, involving the *z*-axis scan data was employed. In this case, data pertaining to the *z*-axis scans at a fixed position closest to the injection point were used. The relevant calculations were performed at the end of the cooling stage of injection moulding. Total azimuthal integrated intensities were conducted, for SAXS images of the type shown in Figure 3.4 above, and for the individual 1<sup>st</sup> order and  $\sqrt{3}$  diffraction patterns corresponding to the skin oriented layers alone. The sum of the latter was divided by the former. This method can yield an estimate of the volume fraction of material present, under the constant volume assumption among other assumptions employed in X-ray diffraction analysis. The method was also employed when monitoring the evolution of skin fraction during flow.

The values of the skin fractions estimated by use of the 3 methods, lied to within 15 % of one another. This was reasonable, considering the uncertainties related with the assumptions employed in X-ray diffraction analysis [25, 26].

Previous work conducted by the Structured Materials group, employed several fluid dynamics and microstructure orientation models to predict the thickness of skin and core oriented cylindrical domain layers in injection moulded SEPS samples [27]. Samples analysed in this thesis were exposed to much higher shear rates during manufacturing. However, *Q* during injection moulding was relatively low at  $0.35 \text{ cm}^3 \text{ s}^{-1}$ . In addition, the samples were sufficiently thin so that the isothermal injection moulding conditions during the filling stage can be regarded as a reasonable approximation.

As a first attempt in predicting the core oriented cylindrical domain thickness of the samples analysed, the 2 simplest models described in the form of generalised Newtonian relations were employed. To supplement these models, an orientation model devised by the Structured Materials group was also used. Equations 3.1 and 3.2 depict the form of the velocity gradient tensor,  $\nabla \vec{v}$ , and orientation model employed, respectively, in the analysis [27].

$$\nabla \vec{v} = \frac{3Q}{8\pi r b} \begin{bmatrix} \frac{\partial v_r}{\partial r} & 0 & \frac{\partial v_r}{\partial z} \\ 0 & -\frac{\partial v_r}{\partial r} & 0 \\ 0 & 0 & 0 \end{bmatrix} \quad (3.1)$$

$$\psi = \frac{|\vec{\gamma}_v|}{|\vec{\epsilon}_v|} \quad (3.2)$$

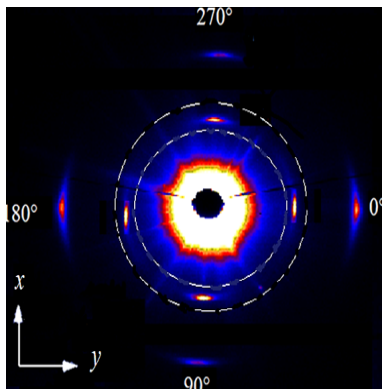
In equation 3.1,  $Q$  denotes the volumetric flowrate of SEPS,  $b$  denotes the half-thickness of the cylindrical disc samples,  $r$  denotes the distance from the injection point and  $\frac{\partial v_r}{\partial r}$  and  $\frac{\partial v_z}{\partial z}$  denote the radial and axial velocity gradients, respectively, modelling the flow of SEPS. In addition, in equation 3.2,  $\psi$  denotes the ratio of the magnitudes of the shear and extensional rate vectors. Details of the methodology and models including the geometry approximation of the flow, can be found in Appendix B.

### 3.2.2 Degree of orientation of cylindrical domains

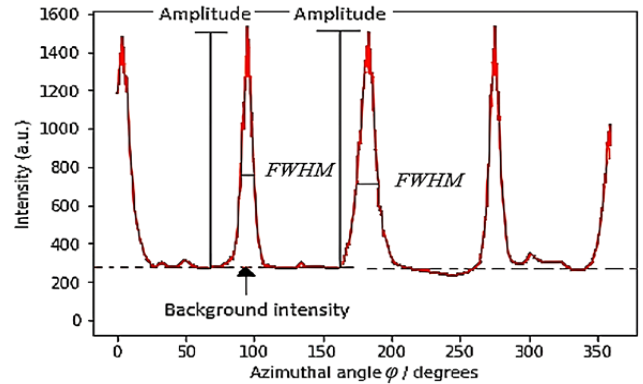
The core and skin oriented cylindrical domains may not be perfectly aligned in their respective directions. It is vital that the SEPS samples, which are potential candidates for use in PHV leaflets, exhibit very good alignment of cylindrical microstructure.

In quantifying the degree of orientation of both skin and core oriented domains, 2 independent methods were employed. It must be noted that, degree of orientation was only estimated for the  $z$ -axis scan data, which are relevant to SAXS measurements during the process of injection moulding.

The first method was that of the Full Width Half Maximum,  $FWHM$ . A  $FWHM$  of  $180^\circ$  corresponds to an isotropic microstructure. The smaller the  $FWHM$ , the better the degree of orientation. Figure 3.5 depicts the methodology employed in calculating the  $FWHM$  [28].



(a)  $z$ -axis scan SAXS image.



(b) Azimuthal integrated intensity.

Figure 3.5: Azimuthal integrated intensity profile (3.5b) for  $z$ -axis X-ray scan (3.5a). The area of integration is enclosed between the dashed lines.

The 2<sup>nd</sup> method was that of Hermans Orientation Factor,  $HOF$ . This method employs integrals of the form in equations 3.3 and 3.4. In computing  $HOF$ , regions corresponding to 1<sup>st</sup> order and  $\sqrt{3}$  diffraction spots for skin and core oriented domains were isolated. DawnDiamond version 2.21, has a processing tool which allows manual masking or coverage of regions in an X-ray diffraction pattern. As a result,  $HOF$  was computed for skin and core diffraction patterns individually [29].

$$HOF = \frac{3 < \cos^2 \phi > - 1}{2} \quad (3.3)$$

$$< \cos^2 \phi > = \frac{\int_0^{2\pi} (I(\phi) \cos^2 \phi \sin \phi) d\phi}{\int_0^{2\pi} (I(\phi) \sin \phi) d\phi} \quad (3.4)$$

In equation 3.4, the integrals were performed over the range  $0^\circ < \phi < 360^\circ$ . In addition,  $I(\phi)$  corresponds to the total azimuthal integrated intensity at a fixed range of polar angles,  $2\theta$ , encompassing both 1<sup>st</sup> order and  $\sqrt{3}$  diffraction spots for skin and core oriented cylindrical domains, respectively. The polar angle,  $2\theta$ , is measured from the centre of the SAXS image in Figure 3.5. Values of  $HOF$  of 1, 0 and -0.5 indicate perfect radial, random and circumferential alignment of cylindrical microstructure, respectively [30].

In spite of the fact that, both  $FWHM$  and  $HOF$  methods were used, the results for  $FWHM$  are mainly presented in this thesis. The reason for preferring  $FWHM$  over  $HOF$  is because, the latter may be more sensitive to any remaining intensity noise in the data, as it involves a ratio of integrals over a range of  $\phi$  values.

### 3.2.3 $d$ -spacing of cylindrical domains

Sufficient insight into residual stresses resulting from the process of injection moulding can be acquired by measuring the  $d$ -spacing of core and skin oriented cylindrical domains [31].

As far as this thesis is concerned,  $d$ -spacing was calculated for both 1<sup>st</sup> order and  $\sqrt{3}$  diffraction intensity peaks, in DawnDiamond version 2.21, for the  $z$ -axis scan data.

In theory, any of the  $d$ -spacings of 1<sup>st</sup> order and  $\sqrt{3}$  diffraction patterns can be calculated, to gain insight into the effects injection moulding has on the stresses sustained by the cylindrical SEPS discs. If the wavelength,  $\lambda$ , of the X-ray radiation is specified, Bragg's law can be used to calculate the  $d$ -spacing between different sets of parallel atomic closed packed planes. Bragg's law is depicted in equation 3.5 [32].

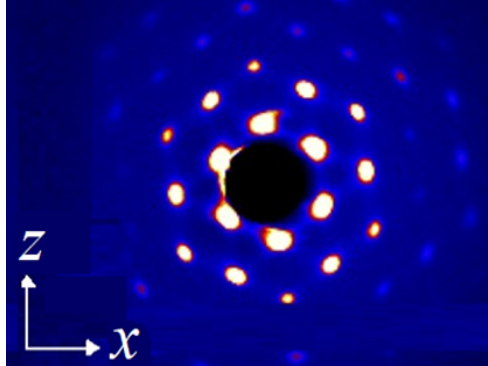
$$m\lambda = 2d_{(hkl)} \sin \theta \quad (3.5)$$

In equation 3.5,  $m$  refers to the order of the X-ray intensity diffraction pattern, and  $d_{(hkl)}$  refers to the spacing between sets of parallel atomic closed packed planes defined by the Miller indices  $h$ ,  $k$  and  $l$  [32].

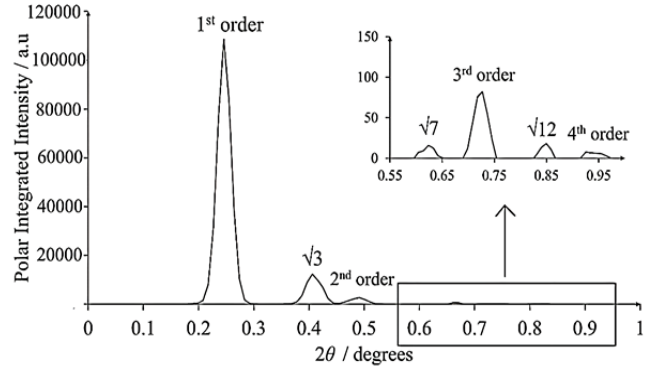
The  $d$ -spacings of both  $\sqrt{3}$  and 1<sup>st</sup> order X-ray diffraction intensity patterns were calculated. The  $d$ -spacings of the  $\sqrt{3}$  X-ray diffraction patterns were multiplied by a factor of  $\sqrt{3}$ , and plotted together with the relevant  $d$ -spacings of 1<sup>st</sup> order diffraction patterns. This was performed to ensure that, Bragg's law was obeyed and the calculations were reliable [32].

In addition, with regard to the microfocus data, use of Bragg's law allowed determination of the order,  $m$  of the diffraction peaks observed in polar integrated intensity curves. Figure 3.6, depicts a typical hexagonal diffraction pattern.

Moreover, Figure 3.6 shows a plot of polar integrated intensity against  $2\theta$ , and the corresponding order of the peaks observed. Assignment of the order of each peak was performed by, measuring the  $d$ -spacing of the 1<sup>st</sup> order intensity peak first. In the case of Figure 3.6, this was measured at 209.8 Å, and  $\lambda$  was specified by the Synchrotron facility at 0.9 µm [33].



(a)  $y$ -axis scan SAXS image, mid-sample.



(b) Polar integrated intensity plot.

Figure 3.6: (3.6a) depicts a  $y$ -axis scan SAXS image, mid-way across the thickness of a sample. (3.6b) depicts a polar integrated intensity plot for the SAXS image in (3.6a).  $2\theta$  is measured from the centre of the SAXS image in (3.6a).

Figure 3.6 demonstrates that, the cylindrical microstructure attained extremely good orientation. Peaks of order up to  $m = 4$  were observed, meaning extremely good alignment of sets of parallel crystallographic, atomic closed-packed planes.

# Chapter 4

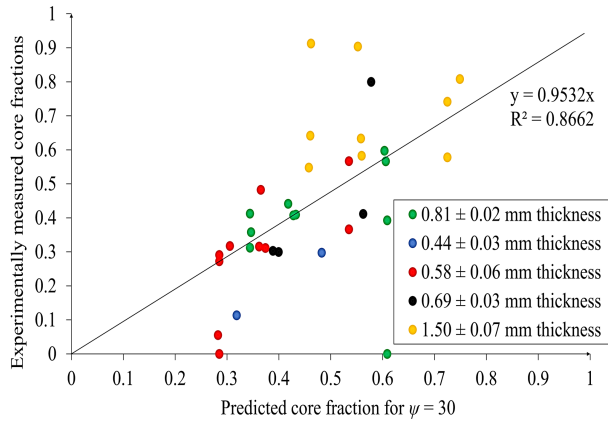
## Results and discussion

### 4.1 Skin and core oriented cylindrical domains

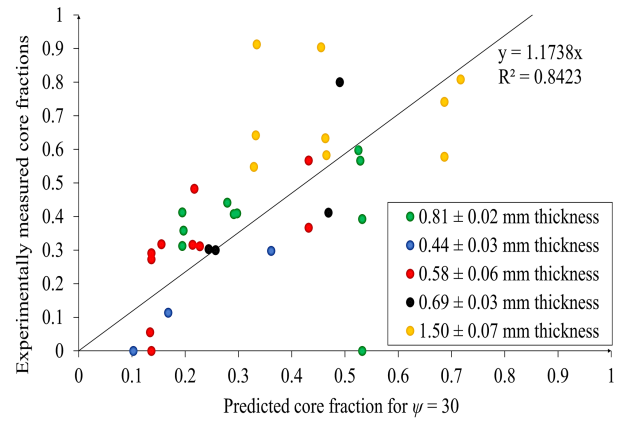
#### 4.1.1 Experimentally determined and predicted volume fractions

The experimentally determined skin layer fractions, for the samples detailed in Table 5.1 of Appendix A, were plotted against their predicted values for the generalised Newtonian constitutive relations. The plots are shown in Figure 4.1.

The critical  $\psi = 30$  employed, represents the value at which transition from core to skin oriented domains occurs, across the thickness of the samples. It was determined in previous studies conducted by the Structured Materials group [6].



(a) Power law, with  $n = 0.53$ .



(b) Simple Newtonian.

Figure 4.1: (4.1a) and (4.1b) depict linear regression plots, in the case of the power law and simple Newtonian models, respectively.  $n = 0.53$  was determined for the power law model by, optimising the linear regression coefficient,  $R^2$ , at specified  $\psi = 30$ .

In spite of the fluid dynamics complexity of the injection moulding process and viscoelastic rheological behaviour of SEPS, both generalised Newtonian models performed satisfactorily. This may well be due to the low  $Q$  of  $0.35 \text{ cm}^3 \text{ s}^{-1}$ , during injection moulding. The  $R^2$  values are offset from the value of 1 by at least 0.14. Uncertainties related to the experimentally determined skin layer fractions and the simplifying assumptions of the models, both influence this outcome.

Molten SEPS has been experimentally proven, using rotational rheometry, to be shear thinning [6]. The optimal  $n$  of 0.53 for the power law model agrees with this. However, a sensitivity analysis was also conducted for the power law model by, determining the sets of  $\psi$  and  $n$  that optimise the  $R^2$  in the linear regression plots of Figure 4.1. Figure 4.2 depicts the resultant  $R^2$ , for each optimal set of parameters.

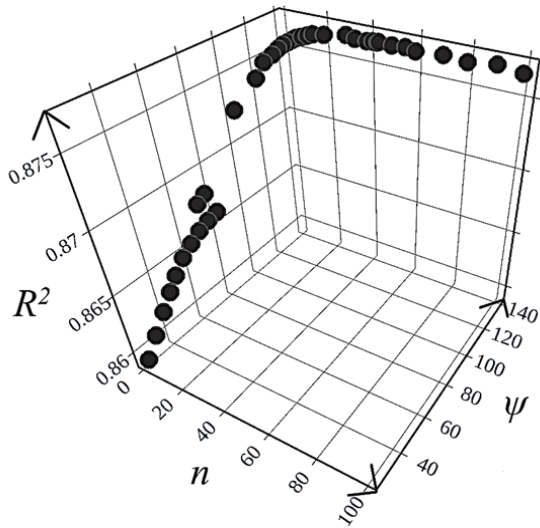


Figure 4.2: 3D scatter plot of  $n$  and  $\psi$  combinations that optimise  $R^2$  of the linear regression plots .

Figure 4.2, demonstrates that, shear thickening behaviour also optimises  $R^2$ . However, the differences between optimal  $R^2$ , in each scenario, are minor. The uncertainties underlying the experimentally determined skin layer fractions, constrain the optimal  $R^2$  in the range of  $0.86 < R^2 < 0.88$ . This demonstrates that, the power law model with  $n = 0.53$  at specified  $\psi = 30$ , yielding  $R^2 = 0.866$ , is a sufficiently good model, given that SEPS was experimentally determined to be shear thinning [6],

#### 4.1.2 Influence of processing parameters on skin layer volume fraction

The main focus of the discussion will be on annealing and cooling conditions which, can be easily adjusted during injection moulding.

As far as the microfocus data are concerned, Figures 4.3 and 4.4 depict the experimentally determined skin layer fractions at different annealing conditions, for the data in Tables 5.1 and 5.2 in Appendix A, respectively.

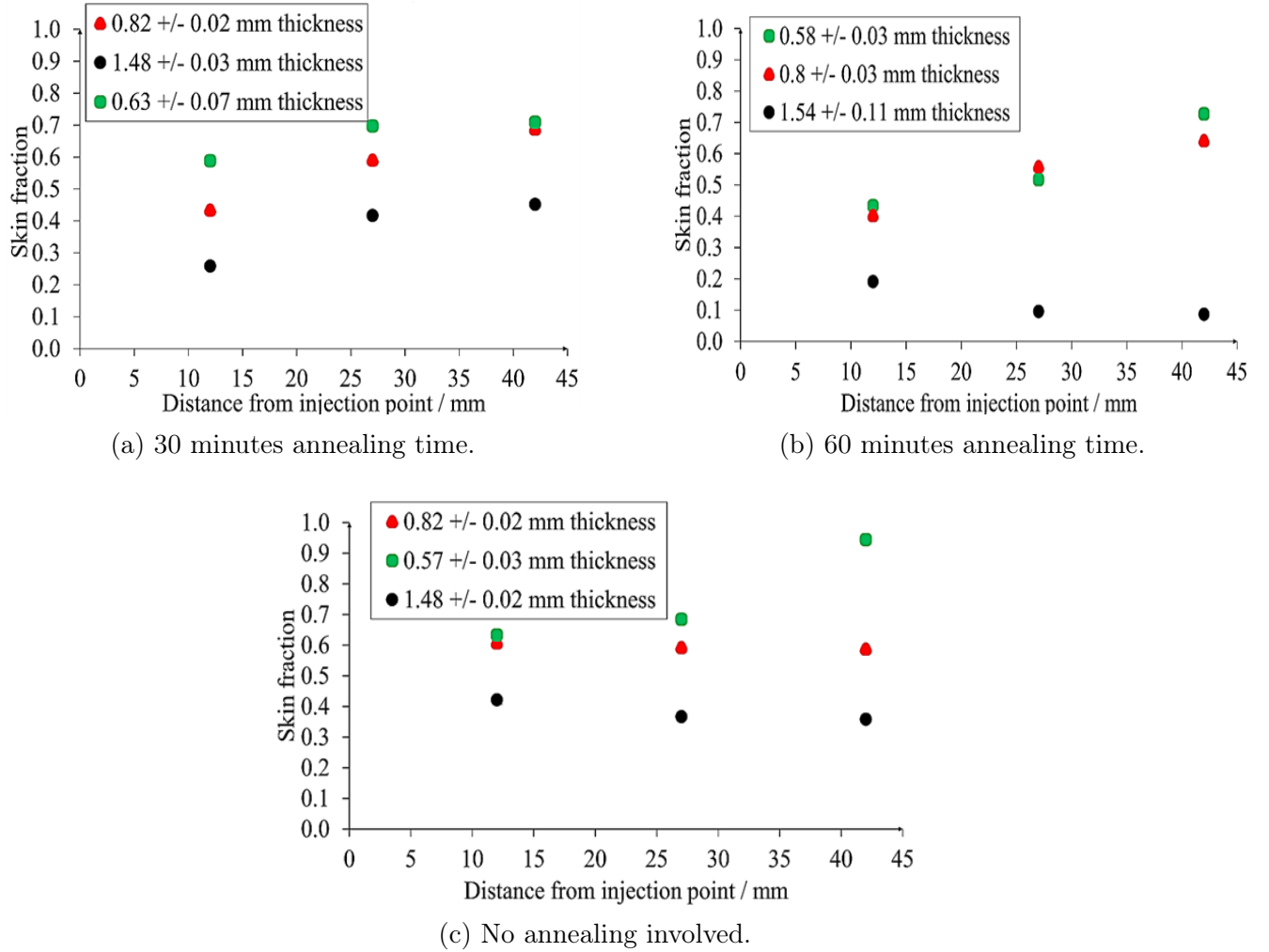


Figure 4.3: (4.3a), (4.3b), (4.3c), are skin layer fractions against distance from injection point, for different annealing conditions. The plots are relevant to the *x*-axis scan data.

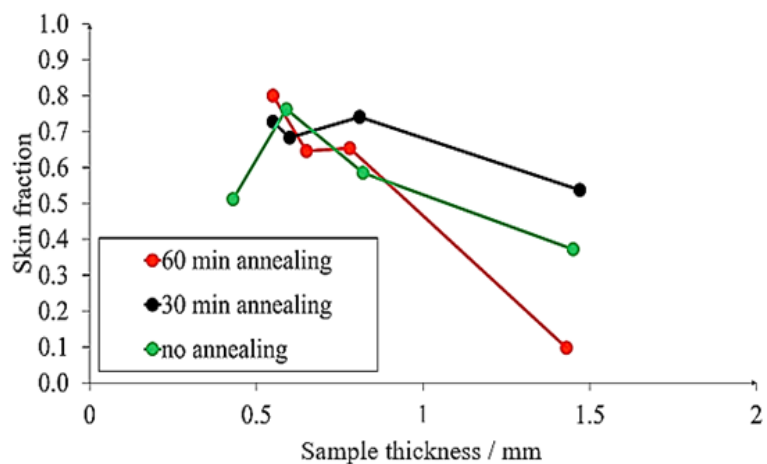


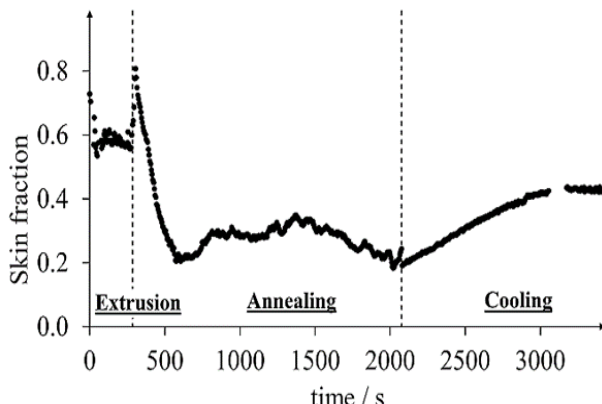
Figure 4.4: Plot of skin layer fraction against sample thickness, for different annealing conditions. The plot is relevant to the *y*-axis scan data.

In general, different annealing conditions were observed not to significantly affect the skin fraction attained by different injection moulded samples, post-cooling. However, upon more thorough analysis of the results, it was observed that, annealing time had the most influence on the skin layer fraction attained, post-cooling, for the thickest samples. This also lies in accordance with what is depicted in Figures 4.3 and 4.4.

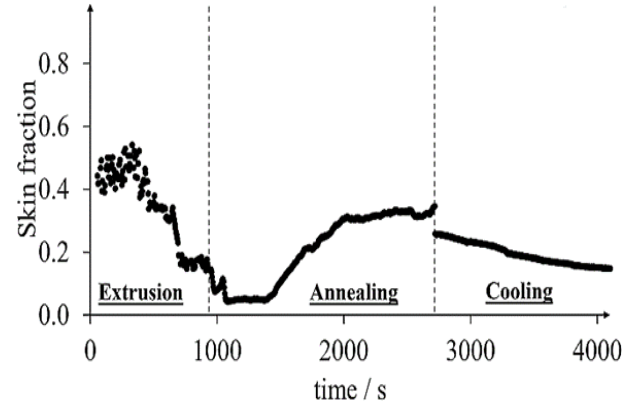
Thicker SEPS samples, are associated with smaller average shear rates, during flow. Figure 4.4 above, demonstrates that, skin layer fraction decreased with increasing sample thickness, as expected. The decreasing average shear rate, reduced the volume fraction of skin oriented cylinders in each sample.

The reason behind different annealing conditions having the largest effect on skin layer fraction for the thickest samples, is unclear. The presence of lower average shear rates in thicker samples may have allowed for different annealing conditions to exhibit a more observable, unmasked influence on the skin fraction attained, post-cooling.

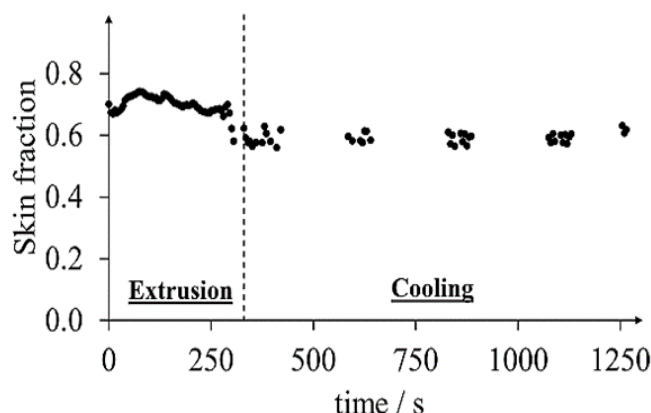
The evolution of skin fraction was also monitored during flow progression of SEPS. Figure 4.5, depicts the experimentally measured skin fractions, for different samples during flow, at the closest position to the injection point.



(a) 0.68 mm sample thickness.



(b) 1.47 mm sample thickness.



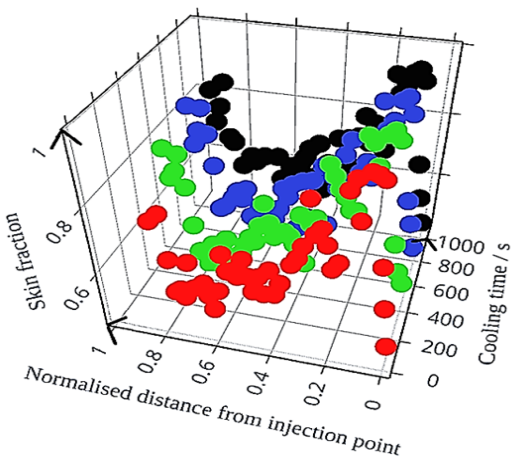
(c) 0.6 mm sample thickness.

Figure 4.5: (4.5a) and (4.5b) include a 30 minutes annealing stage. On the contrary, (4.5c) does not involve annealing.

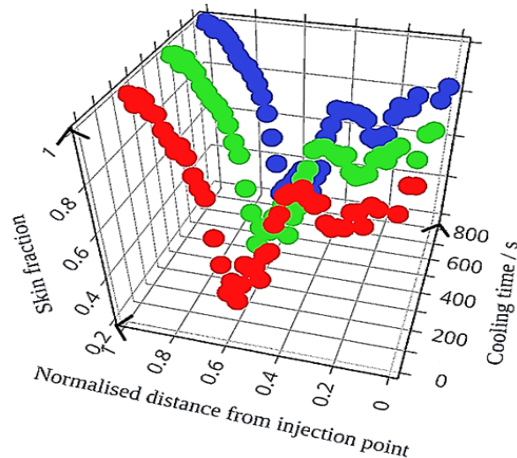
According to Figure 4.5, regardless of whether annealing time at a fixed temperature of 453 K was incorporated in the injection moulding process, the thickness of the injection moulded samples played a more significant role in determining how the skin fraction evolved during the cooling stage.

There seems to be a transition in evolution of skin fraction from an increasing to a decreasing trend, from thinner to thicker samples, according to Figure 4.5. This is clearly demonstrated between the 0.68 mm and 1.47 mm thick samples. The reason may be due to, differences in cooling rates. Thicker samples are associated with lower cooling rates. Cooling time was 20 minutes on average, and the temperature, post-cooling, was approximately 323 - 338 K. This lies below the glass transition temperature,  $T_g = 373$  K, of the styrene cylinders in SEPS [13]. The dynamics of the cooling rate were more significant compared to those of different annealing conditions, during injection moulding.

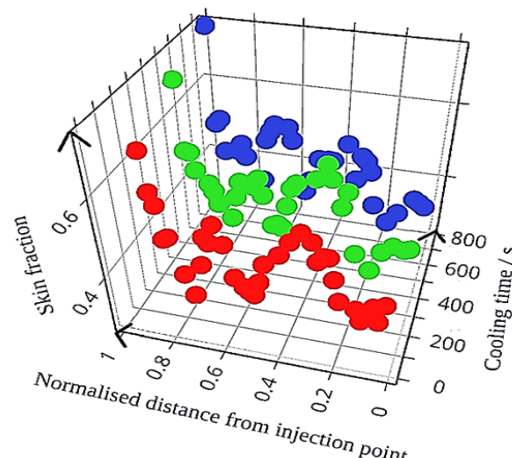
The evolution of skin fraction was also monitored as a function of distance from injection point and cooling time. Figure 4.6 below, depicts results pertaining to this analysis.



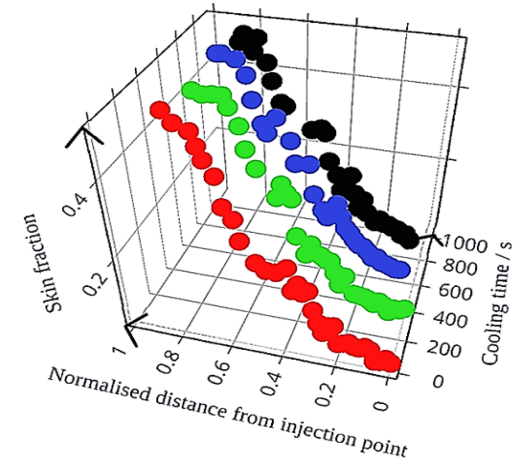
(a) 0.58 mm sample thickness.



(b) 0.72 mm sample thickness.



(c) 0.8 mm sample thickness.



(d) 1.54 mm sample thickness.

Figure 4.6: In (4.6a), (4.6b), (4.6c) and (4.6d), the relevant samples were first exposed to 60 minutes annealing at 453 K.

In Figure 4.6, above, it is clear that, for all relevant samples, skin layer fraction, did not significantly change with cooling time as much as it did with distance from injection point. Figure 4.6 shows that, the skin layer fraction went through minima and maxima, across the radius of each sample. This oscillatory behaviour became less observable, as sample thickness increased. The higher average shear rates associated with thinner samples may have promoted observation of this phenomenon, which became increasingly masked, as sample thickness increased.

## 4.2 Degree of orientation of cylindrical domains

### 4.2.1 Influence of processing parameters on degree of orientation

In quantifying the degree of orientation of skin and core oriented styrene glassy domains, the *FWHM* method was mainly employed. Degree of orientation was quantified only during the process of injection moulding.

The method of Hermans Orientation Factor, *HOF*, was used to confirm that skin oriented domains yield a value of  $HOF = 1$  and core oriented domains yield a value of  $HOF = -0.5$ , approximately. Figure 4.7 depicts *HOF* plots for core and skin oriented domains, for two different SEPS samples.

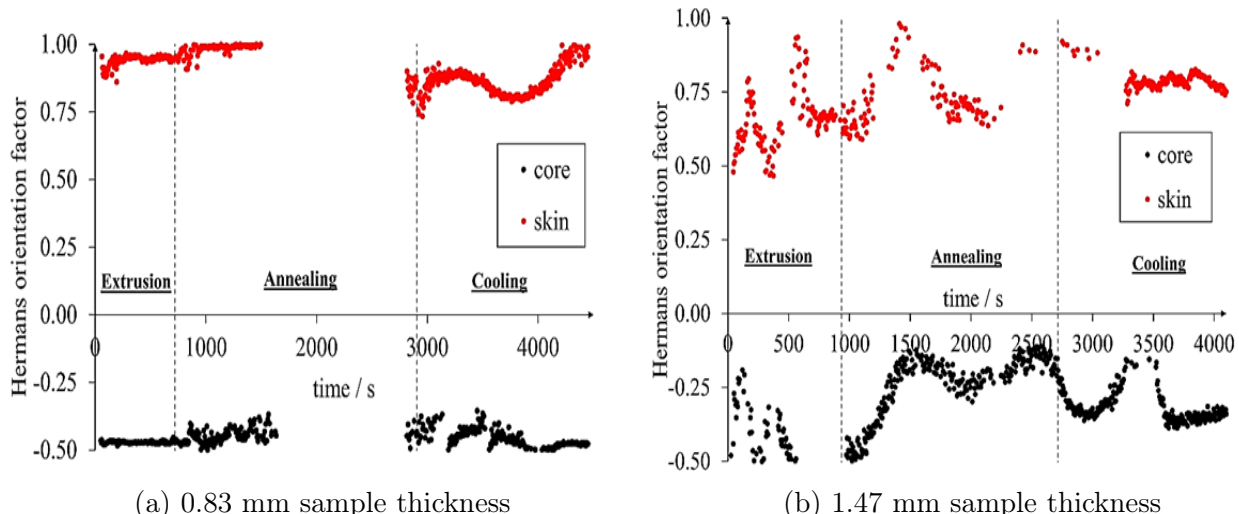
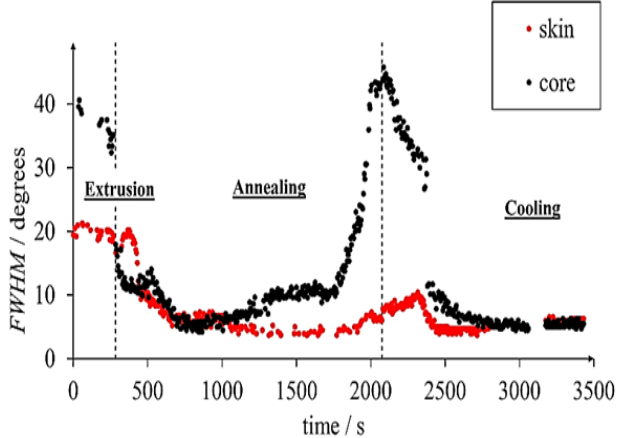
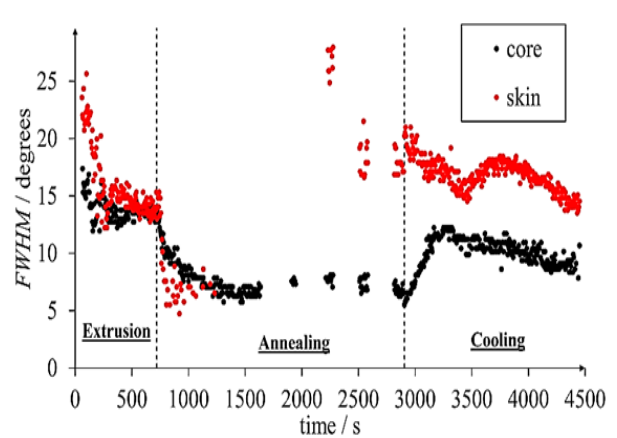


Figure 4.7: *HOF* plots of core and skin oriented cylindrical domains, for two different sample thicknesses.

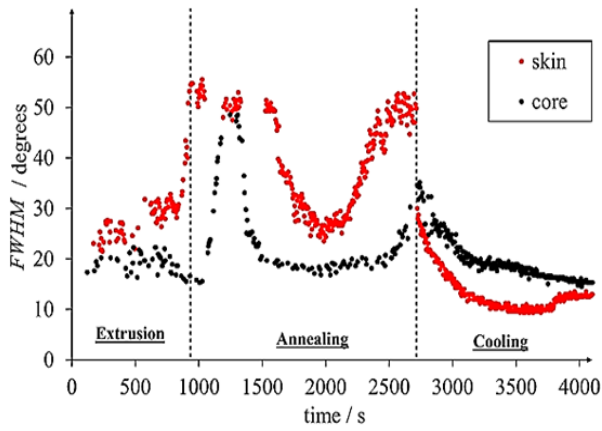
As far as the *FWHM* method is concerned, Figure 4.8 depicts *FWHM* plots of core and skin oriented domains, for different SEPS sample thicknesses.



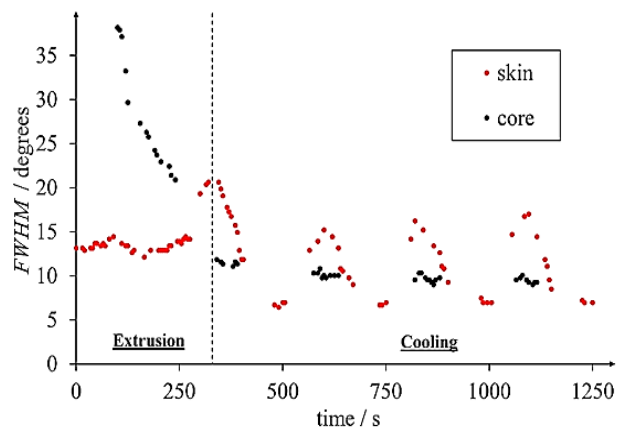
(a) 0.68 mm sample thickness.



(b) 0.83 mm sample thickness.



(c) 1.47 mm sample thickness.



(d) 0.6 mm sample thickness.

Figure 4.8:  $FWHM$  calculations for different sample thicknesses.

According to Figure 4.8, all relevant samples displayed extremely good alignment of core and skin oriented cylindrical domains, by the end of the cooling stage.

On all occasions, the  $FWHM$  was always less than  $20^\circ$ , post-cooling. This signifies that there were minor differences in degree of orientation of cylindrical domains between samples of different thickness.

Furthermore, the SEPS sample with a thickness of 0.6 mm which was not subjected to annealing during injection moulding, also displayed extremely good cylindrical domain orientation, by the end of the cooling stage. This shows that, annealing temperature and annealing time may not have significantly contributed to the degree of orientation of the cylindrical microstructure in SEPS samples, post-injection moulding.

However, it must be noted that, the 0.6 mm thickness sample was also exposed to the largest average shear rates as opposed to the other samples displayed in Figure 4.8. This may in theory, be in favour of improvements in orientation of the skin layer. In spite of this fact, the core layer of this particular sample, also exhibited extremely good alignment, post-cooling.

## 4.3 $d$ -spacing of cylindrical domains

### 4.3.1 Influence of processing parameters on $d$ -spacing

The evolution of  $d$ -spacing for both skin and core layers was monitored during flow progression of SEPS. It was observed that, on average, the  $d$ -spacing of the skin layer decreased as the process of injection moulding progressed. On the contrary, that of the core layer increased, on average. Figure 4.9, depicts the experimentally measured  $d$ -spacings, for different samples during flow, as measured at the closest position to the injection point.

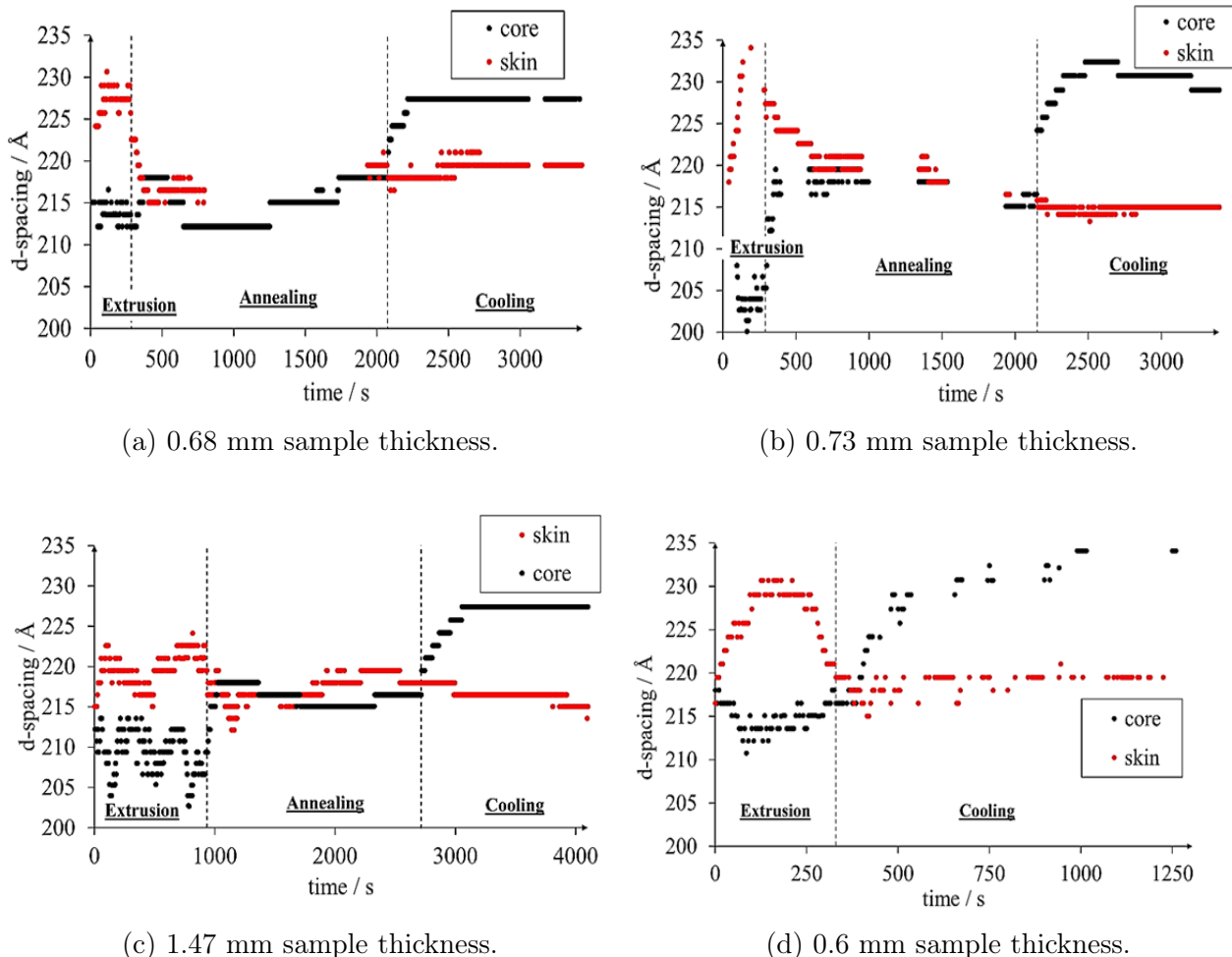


Figure 4.9: (4.9a),(4.9b) and (4.9c) depict plots of  $d$ -spacings for both skin and core oriented cylindrical domains for SEPS samples that were also annealed. In the case of (4.9d), the SEPS sample was not annealed.

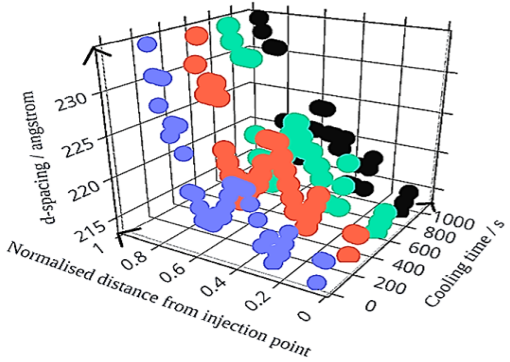
$d$ -spacing for both skin and core layers varied negligibly during the process of annealing, as also demonstrated in Figure 4.9. This lies in accordance with what the literature predicts, with reference to diblock styrene-based TBCPs [20].

Annealing can assist with relieving residual stresses, during the process of injection moulding. Regardless of whether the process of annealing was present or not, the  $d$ -spacing of the core

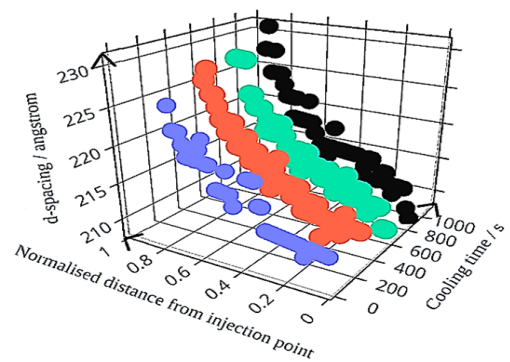
layer was observed to increase during the cooling stage, as demonstrated in Figure 4.9. This is indicative of expansion, as far as the core layer is concerned. The expansion could have been caused by stretching of the core layer during solidification of the material. It is expected that the external surfaces solidify first, and this can cause some stresses on the middle layer, which solidifies last.

In spite of all the aforementioned observations,  $d$ -spacing for both skin and core layers did not vary significantly between the extrusion and the end of cooling stages. This signifies that, the SEPS samples did not have significant residual stresses, which is desirable for use in polymeric heart valve leaflets. Residual stresses tend to reduce the durability of the material.

$d$ -spacing was also monitored as a function of distance from injection point and cooling time. The evolution of  $d$ -spacing for core layers was observed to go through maxima and minima across the radius of each sample. It did not vary as significantly, with cooling time. This observation bears resemblance to that made for the volume fraction of skin oriented cylindrical domains in Figure 4.6. Figures 4.10 and 4.11 depict this observation.

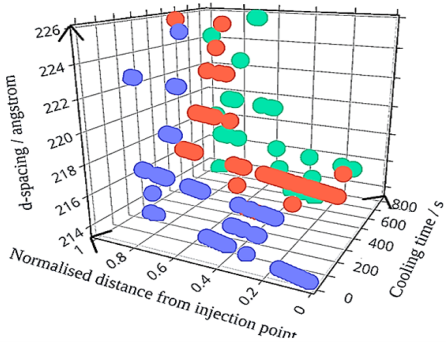


(a) 0.58 mm thickness sample.

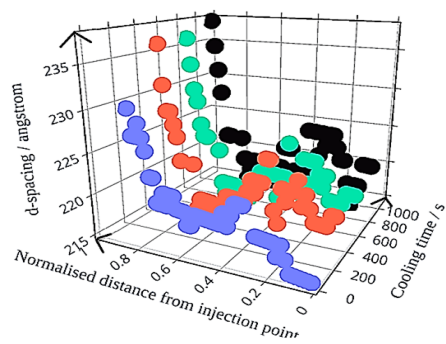


(b) 1.54 mm thickness sample.

Figure 4.10: 3D scatter plots of  $d$ -spacing of core layer as a function of distance from injection point and cooling time. In both (4.10a) and (4.10b), the SEPS samples were also annealed at 453 K for 60 minutes.



(a) 0.43 mm thickness sample.



(b) 1.45 mm thickness sample.

Figure 4.11: 3D scatter plots of  $d$ -spacing of core layer as a function of distance from injection point and cooling time. In both (4.11a) and (4.11b), the SEPS samples were not subjected to annealing.

# Chapter 5

## Conclusions and recommendations

### 5.1 Conclusions

The microstructural characteristics of a TBCP intended for use in polymeric heart valve prostheses were analysed, during the process of injection moulding and post-injection moulding. Aspects such as, degree of orientation of cylindrical styrene hard domains and any associated residual stresses in resultant material microstructure, were examined.

Annealing time, was observed to have minimal influence on the final microstructural characteristics of the injection moulded disc samples. It could be significantly reduced thus, minimising the manufacturing time of the polymeric heart valve leaflets.

The most significant parameter in the injection moulding process, as far as degree of orientation, *d*-spacing and skin layer volume fraction are concerned, was the cooling rate and hence thickness of the TBCP samples prepared.

The polymeric heart valve leaflets must demonstrate both anisotropy in mechanical properties as well as, anisotropy in microstructure orientation. The negligible residual stresses, and excellent degree of orientation suggest that, these anisotropic properties can be attained in a product that embodies the TBCP SEPS, manufactured by the process of injection moulding.

### 5.2 Recommendations

Future studies should examine more closely the bio-stability and bio-compatibility of SEPS, against other polymer candidates for use in polymeric heart valve leaflets.

The technique of birefringence could also be used in future work. The technique has been demonstrated to isolate the flow induced stresses which are in general, orders of magnitude larger than the thermally induced stresses [20]. This may assist in optimising the volumetric flowrate employed during injection moulding of polymers used in polymeric heart valve leaflets.

Furthermore, it is recommended that Giesekus or 3<sup>rd</sup> order fluid viscoelastic constitutive relations are used in future studies, to predict the skin layer fraction attained after the process of injection moulding. High shear rates present during the injection moulding of SEPS, necessitate use of a viscoelastic constitutive relation that employs a convected coordinate system. The relaxation time for polymer chains of SEPS, is unlikely to be lower than the reciprocal of the shear rates encountered during the injection moulding process.

# References

- [1] Eric Van Belle et al. “von Willebrand Factor and Management of Heart Valve Disease: JACC Review Topic of the Week”. eng. In: *Journal of the American College of Cardiology* 73.9 (2019), pp. 1078–1088. ISSN: 0735-1097.
- [2] Peter Zilla et al. “Prosthetic heart valves: Catering for the few”. eng. In: *Biomaterials* 29.4 (2007), pp. 385–406. ISSN: 0142-9612.
- [3] M H Yacoub and J J M Takkenberg. “Will heart valve tissue engineering change the world?” eng. In: *Nature clinical practice cardiovascular medicine* 2.2 (2005), pp. 60–61. ISSN: 1743-4297.
- [4] Mike Mitka. “Final Report on Mechanical vs Bioprosthetic Heart Valves”. eng. In: *JAMA : the journal of the American Medical Association* 283.15 (2000), pp. 1947–1948. ISSN: 0098-7484.
- [5] G Burriesci, F. Cavallo Marincola, and C Zervides. “Design of a novel polymeric heart valve”. eng. In: *Journal of medical engineering technology* 33.1 (2010), pp. 7–22. ISSN: 0309-1902.
- [6] Joanna Stasiak et al. “A bio-inspired microstructure induced by slow injection moulding of cylindrical block copolymers”. eng. In: *Soft matter* 10.32 (2014), pp. 6077–6086. ISSN: 1744-683X.
- [7] Anwarul Hasan et al. “Biomechanical properties of native and tissue engineered heart valve constructs”. eng. In: *Journal of biomechanics* 47.9 (2013), pp. 1949–1963. ISSN: 0021-9290.
- [8] M Serrani et al. “A Computational Tool for the Microstructure Optimization of a Polymeric Heart Valve Prosthesis”. eng. In: *Journal of biomechanical engineering* 138.6 (2016), pp. 061001–061001. ISSN: 0148-0731.
- [9] Joanna R Stasiak et al. “Correction: Design, development, testing at ISO standards and in vivo feasibility study of a novel polymeric heart valve prosthesis”. eng. In: *Biomaterials science* 8.16 (2020), pp. 4639–4639. ISSN: 2047-4830.
- [10] Feng Guo et al. “Bio-inspired anisotropic polymeric heart valves exhibiting valve-like mechanical and hemodynamic behavior”. eng. In: *Science China materials* 63.4 (2020), pp. 629–643. ISSN: 2095-8226.
- [11] Thomas E Claiborne et al. “Polymeric trileaflet prosthetic heart valves: evolution and path to clinical reality”. eng. In: *Expert review of medical devices* 9.6 (2012), pp. 577–594. ISSN: 1743-4440.
- [12] Zhaobo Wang. “Mechanical properties, Payne effect, and Mullins effect of thermoplastic vulcanizates based on high-impact polystyrene and styrene–butadiene rubber compatibilized by styrene–butadiene–styrene block copolymer”. eng. In: *Journal of thermoplastic composite materials volume 28 issue 8 page 1154* ().

- [13] Rameshwar Adhikari et al. “Correlation between Molecular Architecture, Morphology, and Deformation Behaviour of Styrene/Butadiene Block Copolymers”. eng. In: *Macromolecular chemistry and physics* 204.3 (2003), pp. 488–499. ISSN: 1022-1352.
- [14] Joanna R. Stasiak et al. “Design, development, testing at ISO standards and in vivo feasibility study of a novel polymeric heart valve prosthesis”. In: *Biomaterials Science* 8.16 (2020), pp. 4467–4480. DOI: 10.1039/d0bm00412j.
- [15] Shinichi Sakurai. “Recent developments in polymer applications of synchrotron small-angle X-ray scattering”. eng. In: *Polymer international* 66.2 (2017), pp. 237–249. ISSN: 0959-8103.
- [16] A Ramazani S.A and M Kanvisi. “Modeling of Viscoelastic Fluid Flow Behavior in the Circular Die Using the Leonov-Like Conformational Rheological Constitutive Equations”. eng. In: *Macromolecular symposia*. 274.1 (2008), pp. 6–10. ISSN: 1022-1360.
- [17] A.M. Flaman. *Build-up and relaxation of molecular orientation in injection moulding, PhD thesis 1990*. URL: <https://doi.org/10.6100/IR339750>. (accessed: 26.04.2021).
- [18] Xiaoshi Jin. “Boundary element study on particle orientation caused by the fountain flow in injection molding”. eng. In: *Polymer engineering and science* 33.19 (1993), pp. 1238–1242. ISSN: 0032-3888.
- [19] Evan Mitsoulis. “Fountain flow revisited: The effect of various fluid mechanics parameters”. eng. In: *AICHE journal* 56.5 (2010), pp. 1147–1162. ISSN: 0001-1541.
- [20] Mohit Mamodia et al. “Effect of Microdomain Structure and Process Conditions on the Mechanical Behavior of Cylindrical Block Copolymer Systems”. eng. In: *Macromolecules* 40.20 (2007), pp. 7320–7328. ISSN: 0024-9297.
- [21] Daisuke Yamaguchi et al. “Effect of Annealing on the Perfection of Ordered Structure of Highly Asymmetric Diblock Copolymer”. eng. In: *Macromolecules* 32.22 (1999), pp. 7696–7699. ISSN: 0024-9297.
- [22] Bin Su Yong-sheng Zhao. “Effect of Microdomain Structure on the Mechanical Behavior of Binary Blends”. eng. In: *Chinese journal of polymer science* 33.7 (2015), pp. 964–975. ISSN: 0256-7679.
- [23] Diamond light source. *Welcome to I22*. URL: <https://www.diamond.ac.uk>. (accessed: 26.04.2021).
- [24] Norihiro Sota et al. “Directed Self-Assembly of Block Copolymers into Twin BCC-Sphere: Phase Transition Process from Aligned Hex-Cylinder to BCC-Sphere Induced by a Temperature Jump between the Two Equilibrium Phases”. eng. In: *Macromolecules* 46.6 (2013), pp. 2298–2316. ISSN: 0024-9297.
- [25] B. L. Dutrow et. al. *X-ray powder diffraction*. URL: [https://serc.carleton.edu/research\\_education/geochemsheets/techniques/XRD.html](https://serc.carleton.edu/research_education/geochemsheets/techniques/XRD.html). (accessed: 26.04.2021).
- [26] A. A. Kovalev et. al. *Application of X-ray Diffraction Methods to Studying Materials*. URL: <https://doi.org/10.1134/S0036029517130110>. (accessed: 26.04.2021).
- [27] Brubert Jacob. *A novel polymeric prosthetic heart valve: design, manufacture, and testing, PhD Thesis 2016*. URL: <https://doi.org/10.17863/CAM.248>. (accessed: 01.02.2021).

- [28] Joanna Stasiak et al. “Effect of Stretching on the Structure of Cylinder- and Sphere-Forming StyreneIsopreneStyrene Block Copolymers”. eng. In: *Macromolecules* 42.14 (2009), pp. 5256–5265. ISSN: 0024-9297.
- [29] University of Cincinnati Engineering Research Center. *Deformation Morphologies and Toughening of Polymer Systems*. URL: <http://www.eng.uc.edu/~beaucag/Classes/Morphology/Chapter3html>. (accessed: 01.02.2021).
- [30] J. L. White et. al. *The specification of orientation and its development in polymer processing*. URL: <https://doi.org/10.1002/pen.760230503>. (accessed: 01.02.2021).
- [31] UK National Physical Laboratory. *Determination of residual stresses by X-ray diffraction - Issue 2*. URL: <https://eprintspublications.npl.co.uk>. (accessed: 01.02.2021).
- [32] C. J Humphreys. “The significance of Bragg’s law in electron diffraction and microscopy, and Bragg’s second law”. eng. In: *Acta crystallographica. Section A, Foundations of crystallography* 69.1 (2013), pp. 45–50. ISSN: 0108-7673.
- [33] A S Sukhikh, T V Basova, and S A Gromilov. “The use of 2D diffractometry data for oriented samples in the choice of a unit cell”. eng. In: *Journal of structural chemistry* 58.5 (2017), pp. 953–963. ISSN: 0022-4766.
- [34] Marc Peter Deisenroth. *Mathematics for machine learning / Marc Peter Deisenroth, A. Aldo Faisal, Cheng Soon Ong*. eng. 2020. ISBN: 9781108470049.

# Appendix A

## Thicknesses and annealing conditions of injection moulded SEPS disc samples

Table 5.1: List of sample thicknesses and annealing conditions for *x*-axis scan data.

<b>Sample thickness / mm</b>	<b>Annealing Temperature / K</b>	<b>Annealing time / minutes</b>
0.44 +/− 0.03	453	Not applicable
0.57 +/− 0.03	453	Not applicable
0.58 +/− 0.03	453	60
0.61 +/− 0.07	453	30
0.65 +/− 0.09	453	30
0.72 +/− 0.11	453	60
0.80 +/− 0.03	453	60
0.82 +/− 0.02	453	Not applicable
0.82 +/− 0.02	453	30
1.48 +/− 0.03	453	30
1.48 +/− 0.02	453	Not applicable
1.54 +/− 0.11	453	60

Table 5.2: List of sample thicknesses and annealing conditions for *y*-axis scan data.

<b>Sample thickness / mm</b>	<b>Annealing Temperature / K</b>	<b>Annealing time / minutes</b>
0.43	453	Not applicable
0.59	453	Not applicable
0.55	453	60
0.60	453	30
0.65	453	30
0.78	453	60
0.80	453	60
0.82	453	Not applicable
0.81	453	30
1.47	453	30
1.45	453	Not applicable
1.43	453	60

# Appendix B

## Orientation model

The extensional rate and shear rate vectors  $\vec{\epsilon}_v$  and  $\vec{\gamma}_v$ , respectively, were computed using vectorial analysis [27].

The extensional rate components of the velocity gradient tensor  $\nabla\vec{v}$ , were extracted by use of equation 5.1. In equation 5.1,  $\text{diag}()$  refers to extraction of the diagonal elements of  $\nabla\vec{v}$ , and  $(\nabla\vec{v} \odot \mathbf{I})$  refers to the element-wise multiplication [34] between matrices  $\nabla\vec{v}$  and  $\mathbf{I}$ .

$$\vec{\epsilon}_v = \text{diag}(\nabla\vec{v} \odot \mathbf{I}) = \begin{bmatrix} \frac{\partial v_r}{\partial r} \\ -\frac{\partial v_r}{\partial r} \\ 0 \end{bmatrix} \quad (5.1)$$

Similarly, the shear rate components of  $\nabla\vec{v}$  were extracted using equations 5.2 and 5.3.

$$\mathbf{G} = \nabla\vec{v} \odot (1 - \mathbf{I}) = \begin{bmatrix} 0 & 0 & \frac{\partial v_r}{\partial z} \\ 0 & 0 & 0 \\ 0 & 0 & 0 \end{bmatrix} \quad (5.2)$$

$$\vec{\gamma}_v = \begin{bmatrix} \sum_{i=1}^3 G_{i1} \\ \sum_{i=1}^3 G_{i2} \\ \sum_{i=1}^3 G_{i3} \end{bmatrix} = \begin{bmatrix} 0 + 0 + 0 \\ 0 + 0 + 0 \\ 0 + 0 + \frac{\partial v_r}{\partial z} \end{bmatrix} \quad (5.3)$$

In equations 5.1 and 5.2,  $\mathbf{I}$  is the 3 by 3 identity matrix. These equations were combined to calculate the ratio of the magnitudes of the shear and extensional rate vectors,  $\psi$ , for 2 generalised Newtonian relations.

## Newtonian velocity profile model

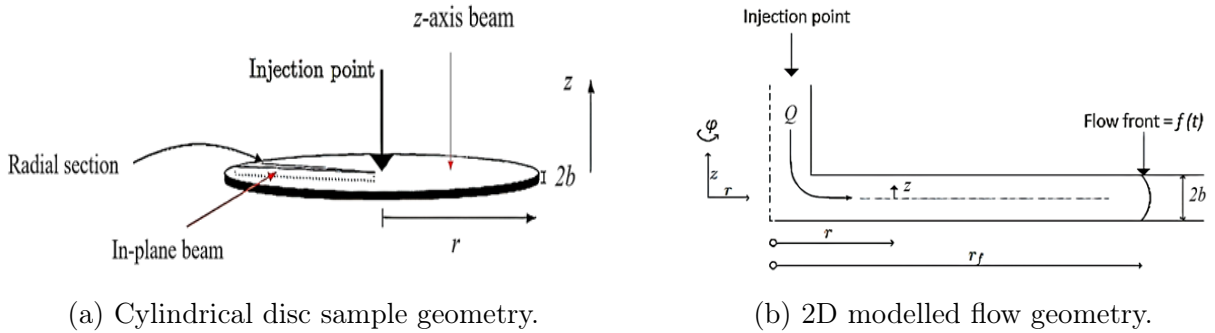


Figure 5.1: (5.1a) and (5.1b) depict the geometry and convention employed in modelling the flow of molten SEPS during injection moulding.

The constitutive relation of the simple Newtonian fluid was employed first. Incompressibility, rotational symmetry and no wall slip were assumed for the geometry depicted in Figure 5.1. Velocities in  $\phi$  and  $z$  directions were set to zero as also shown in equation 5.4. The radial velocity was calculated in the form of equation 5.5.

$$\vec{v} = (v_r(r, z), 0, 0) \quad (5.4)$$

$$v_r = \frac{3Q}{8\pi rb} \left( 1 - \left( \frac{z}{b} \right)^2 \right) \quad (5.5)$$

The velocity gradients in the  $z$  and  $r$  directions were calculated in the form of equations 5.6 and 5.7, respectively.

$$\frac{\partial v_r}{\partial z} = \frac{-3Q}{4\pi rb} \left( \frac{z}{b^2} \right) \quad (5.6)$$

$$\frac{\partial v_r}{\partial r} = \frac{-3Q}{8\pi r^2 b} \left( 1 - \left( \frac{z}{b} \right)^2 \right) \quad (5.7)$$

Similarly the moduli of  $\vec{\gamma}_v$  and  $\vec{\epsilon}_v$  were calculated in the form of equations 5.8 and 5.9.

$$|\vec{\epsilon}_v| = \frac{3Q\sqrt{2}}{8\pi r^2 b} \left( 1 - \left( \frac{z}{b} \right)^2 \right) \quad (5.8)$$

$$|\vec{\gamma}_v| = \frac{3Q}{4\pi rb} \left( \frac{z}{b^2} \right) \quad (5.9)$$

By use of equations 5.8, 5.9 and 3.2, a quadratic in  $z$  was constructed in the form of equation 5.10. The positive root was considered as the physical root. Equation 5.10 was solved for different sample thicknesses,  $2b$ , at different distances from the injection point,  $r$ , to predict the core fraction in each sample.

$$z = -\frac{\sqrt{2}r}{2\psi} + \frac{b}{2\psi}\sqrt{\frac{2r^2}{b^2} + 4\psi^2} \quad (5.10)$$

## Power law velocity profile model

An analysis assuming a power law constitutive relation for SEPS was also conducted. Equations 5.11, 5.12, 5.13, 5.14 and 5.15 were derived for the same parameters as those employed in the simple Newtonian model. In these equations,  $n$  refers to the power law index.

$$v_r(r, z) = \frac{Q}{4\pi br} \left( \frac{2n+1}{n+1} \right) \left( 1 - \left( \frac{z}{b} \right)^{\frac{1+n}{n}} \right) \quad (5.11)$$

$$\frac{\partial v_r}{\partial z} = \frac{-Q}{4\pi rb} \left( \frac{2n+1}{n} \right) z^{\frac{1}{n}} \left( \frac{1}{b} \right)^{\frac{1+n}{n}} \quad (5.12)$$

$$\frac{\partial v_r}{\partial r} = \frac{-Q}{4\pi r^2 b} \left( \frac{2n+1}{n+1} \right) \left( 1 - \left( \frac{z}{b} \right)^{\frac{1+n}{n}} \right) \quad (5.13)$$

$$|\vec{\epsilon}_v| = -\sqrt{2} \frac{Q}{4\pi r^2 b} \left( \frac{2n+1}{n+1} \right) \left( 1 - \left( \frac{z}{b} \right)^{\frac{1+n}{n}} \right) \quad (5.14)$$

$$|\vec{\gamma}_v| = \frac{-Q}{4\pi rb} \left( \frac{2n+1}{n} \right) z^{\frac{1}{n}} \left( \frac{1}{b} \right)^{\frac{1+n}{n}} \quad (5.15)$$

By use of equations 5.14, 5.15 and 3.2, a non-linear equation in  $z$  was constructed in the form of equation 5.16. Equation 5.16 was solved for combinations of  $n$  and  $\psi$ . In each case, the core fraction was predicted. The calculations were performed in VBA in Excel, in this scenario.

$$z^{\frac{1}{n}} \left( \frac{1+n}{n} \right) r \left( \frac{1}{b} \right)^{\frac{1+n}{n}} - \sqrt{2}\psi - \sqrt{2}\psi \left( \frac{z}{b} \right)^{\frac{1+n}{n}} = 0 \quad (5.16)$$

# Nomenclature

$b$	Half-thickness of injection moulded cylindrical SEPS discs	(mm)
$d_{(hkl)}$	Distance between parallel planes of atoms ( $hkl$ )	(Å)
$FWHM$	Full Width Half-Maximum of azimuthal integrated intensity	(°)
$\mathbf{G}$	$2^{\text{nd}}$ order tensor of shear deformation components	( $\text{s}^{-1}$ )
$HOF$	Hermans Orientation Factor	(-)
$h$	$1^{\text{st}}$ Miller index	(-)
$\mathbf{I}$	3 by 3 identity matrix	(-)
$I(\phi)$	X-ray diffraction intensity as a function of azimuthal angle	(a.u.)
$k$	$2^{\text{nd}}$ Miller index	(-)
$l$	$3^{\text{rd}}$ Miller index	(-)
$m$	Order of diffraction pattern as in Bragg's law	(-)
$n$	Power law exponent in power law constitutive relation	(-)
$Q$	Volumetric flowrate of SEPS during injection moulding	( $\text{cm}^3 \text{ s}^{-1}$ )
$R^2$	Linear regression coefficient	(-)
$r$	Radial distance from injection point in cylindrical SEPS discs	(mm)
$t$	Time dimension	(s)
$T_g$	Glass transition temperature	(K)
$T_m$	SEPS melt temperature	(K)
$T_{mould}$	SEPS temperature in aluminium plate mould	(K)
$v_r$	Radial velocity profile	( $\text{m s}^{-1}$ )
$x, y, z$	Cartesian coordinates	(-)
$\nabla \vec{v}$	Velocity gradient 2nd order tensor	( $\text{s}^{-1}$ )
$\frac{\partial v_r}{\partial r}$	Derivative of velocity profile in radial direction	( $\text{s}^{-1}$ )
$\frac{\partial v_r}{\partial z}$	Derivative of velocity profile in axial direction	( $\text{s}^{-1}$ )

$\vec{\gamma}_v$	Shear rate vector	(s <sup>-1</sup> )
$\vec{\epsilon}_v$	Extensional rate vector	(s <sup>-1</sup> )
$\theta$	Polar angle	(°)
$\phi$	Azimuthal angle	(°)
$\psi$	Ratio of magnitudes of shear and extensional rate vectors	(-)